This is a preprint, the final version is subject to change, of the American Mineralogist (MSA)
Cite as Authors (Year) Title. American Mineralogist, in press.
DOI: https://doi.org/10.2138/am-2019-6863

Revision 1 – 12/4/2018

In situ mapping of ferric iron variations in lunar glasses using x-ray absorption spectroscopy

MOLLY C. MCCANTA[1], M.DARBY DYAR[2], ANTONIO LANZIROTTI[3], MATTHEW NEWVILLE[3], LAURA B. BREITENFELD[2]

[1]Department of Earth and Planetary Sciences, University of Tennessee, Knoxville, TN 37996, U.S.A.

[2]Department of Astronomy, Mount Holyoke College, South Hadley, MA 01075, U.S.A.

[3]Center for Advanced Radiation Sources, University of Chicago, 5640 S. Ellis Ave., Chicago, IL 60637, U.S.A.

ABSTRACT

This paper presents a new x-ray absorption spectroscopy (XAS) method for making two-dimensional maps of Fe^{3+} *in situ* in polished glass samples which opens the door to study redox changes associated with magmatic processes such as crystallization, assimilation, ascent, and eruption. Multivariate analysis (MVA) allows selection of specific channels in a spectrum to inform predictions of spectral characteristics. Here, the sparse model of the least absolute shrinkage and selection operator (Lasso) is used to select key channels in XAS channels that can be used to predict accurate in situ Fe^{3+} analyses of silicate glasses. By tuning the model to use only six channels, analytical time is decreased enough to allow mapping of Fe^{3+} variations in samples by making gridded point analyses at the scale of the XAS beam (1-2 μm). Maps of Fe^{3+} concentration can then be constructed using freely available, open source software (http://cars.uchicago.edu/xraylarch/). This result shows the enormous potential of using MVA to select indicative spectral regions for predicting variables of interest across a wide variety of spectroscopic applications. Redox gradients in lunar picritic glass beads first observed with point analyses are confirmed through this XAS mapping and suggest degassing processes during ascent and eruption are responsible for the range of Fe^{3+} values measured in these samples.

INTRODUCTION

Mössbauer reports of Fe^{3+} in lunar glasses and minerals extend back to the time of the Apollo missions themselves (e.g., Hafner et al., 1971; Schürmann and Hafner, 1972; Niebuhr et al., 1973). In contrast, petrologic phase equilibria data on returned samples indicate that the oxygen fugacity (f_{O2}) of the lunar interior is ~IW-1, a reduced region near Fe metal saturation where iron should be predominantly divalent (Sato, 1976). This contradiction persisted for decades until new light was shed on this problem by recent studies (e.g., Saal et al., 2008; McCubbin et al., 2010; Hauri et al., 2011; Hui et al. 2013; Barnes et al. 2014; Füri et al. 2014; Hauri et al. 2015) indicating that the Moon is not as dry as previously thought. Given the potential relationship between hydrogen degassing and oxidation, this recent work re-opens the

question of the presence of Fe^{3+} in lunar glasses. Results of individual point analyses of lunar picritic glass beads indicate they contain 0-25% $Fe^{3+}/\Sigma Fe$ (McCanta et al., 2017); several beads display Fe^{3+} zoning traverses consistent with a late-stage oxidation event.

The presence of Fe^{3+} is significant because it records oxygen potential and thus traces the evolution of oxygen through the parameter of f_{O2} in solar system materials. Quantifying f_{O2} in igneous melts is important for constraining planetary interior physical conditions, but also for investigating potential changes during devolatilization-driven eruptive mechanisms. Historically, quantification of Fe^{3+} in glasses required either wet chemistry or Mössbauer spectroscopy (e.g., Cukierman and Uhlmann, 1974; Huffman et al., 1974; Dyar and Birnie, 1984; Virgo and Mysen, 1985), techniques that require large sample sizes and bulk material. Here we present results of a synchrotron X-ray absorption spectroscopy (XAS) method (cf. Mayhew et al. 2011, Etschmann et al. 2014) for making two-dimensional maps of Fe^{3+} *in situ*, enabling resolution of potential variations at micron scales within the spatial context of coexisting phases. This technique is demonstrated using mapping of lunar glass beads, in which there are varying mechanisms for changing oxidation conditions during magma ascent and eruption.

BACKGROUND

In previous work, a glass calibration for XAS (Dyar et al., 2016a) was developed for Fe^{3+} measurements in silicate glasses, spanning >120 different silicate and redox compositions. It permits accurate *in situ* microscale analyses with an average accuracy of ±3.6 %, similar to that of Mössbauer, by employing a broad spectral range covering the Fe K absorption pre-edge and main edge (7020-7220 eV). This method remains the best method for *in situ* characterization at single point locations on glasses at thin section scales.

However, the 'Holy Grail' of microanalysis is to make two-dimensional maps of Fe^{3+} on thin sections. Because acquiring the full spectral range (300-800 data points) at a single location is time-consuming (ca. 10 minutes), only linear traverses have previously been employed on limited locations, so relevant spatial information may be overlooked. Moreover, traditional methods for predicting Fe^{3+} concentration using XAS, such as those of Wilke et al. (2001) and Cottrell et al. (2009) utilize laborious manual fitting of pre-edge features, making them unrealistic for large numbers of spectra. However, it is undeniably desirable to coregister redox measurements with those of major and minor element concentrations, providing insights into charge balance and diffusion gradients. Therefore, an unbiased, objective method for obtaining redox measurements over two-dimensional arrays was needed to reduce the number of spectral channels and automate the data processing so as to make the duration of data collection practical.

Earlier studies investigating Fe^{3+} *in situ* mapping utilized spectral information collected in the pre-edge region only (Mayhew et al., 2011) or required significant interpolation during data reduction procedures (Muñoz et al., 2006). The mapping method presented in this paper uses the entire XAS spectrum of each glass measured and the multivariate methods developed to deal with the large data volume. In developing the glass Fe^{3+} calibration of Dyar et al. (2016a), one of the models tested was the least absolute shrinkage and selection operator (Lasso) multivariate regression model (Tibshirani 1996; Lanzirotti et al., 2018). It is fundamentally based on the familiar expression for multiple linear regression, $y = \beta_0 + \beta_1 x_1 + \beta_2 x_2 + \ldots + \beta_n x_n$, where y is the weight percent of the oxide of the element being considered, and β_0 and β_i are the regression coefficients for the intercept and each independent channel x_i, respectively. In the XAS data studied here, there are *many* predictor variables, which are the input **X** values (i.e., the matrix of intensity values at each of ~600 channels representing energy) and *relatively few* samples (rows of the **X** matrix). Thus the data exist in a multi-dimensional space in which many

dimensions (wavelength bins) are highly correlated. For example, for any given element, the intensity of many lines will vary together, such as those that collectively make up a single peak.

The Lasso regression shrinks this expression by reducing the number of terms implicitly, constraining the values of the correlation coefficients using the original data matrix **X**. The absolute value of the sum of the β values (correlation coefficients) is constrained by the user to be less than some boundary value *t*. Under this constraint, the model weighs the importance of each channel to the prediction and unimportant channels are driven to β values equal to 0 by an optimization process. Mathematically, this is expressed by Hastie et al. (2009) as:

$$\hat{\beta}^{lasso} = argmin_{\beta} \sum_{i=1}^{N} \left(y_i - \beta_0 - \sum_{j=1}^{p} x_{ij}\beta_j\right)^2 \; subject\ to \; \sum_{j=1}^{p} |\beta_j| \leq t \qquad (1)$$

where $\hat{\beta}^{Lasso}$ is the estimated coefficient in the regression equation, $argmin_{\beta}$ is the value of the vector β that minimizes the squared loss function, y_i is the composition of an individual sample, x_{ij} is intensity at a single channel j for a single sample i, and β_j is the coefficient corresponding to the channel j. In our experience with spectroscopy applications (e.g., Dyar et al., 2012b; Breitenfeld et al., 2018), the Lasso often seems to yield superior results to other regression models because it removes channels due to noise or arising from unrelated spectral features; the same conclusion was reached for other machine learning applications where noise is a problem (Filzmoser et al., 2012). In the application to glass XAS data presented here, the Lasso is used to limit the number of channels to a small enough number to create a redox map in a reasonable acquisition time.

ANALYTICAL METHODS

Major and minor element concentrations in 32 lunar glass beads from Apollo 11 (10084), 14 (14148), and 17 (74220) were analyzed on the Brown University and University of Tennessee Knoxville Cameca SX-100 electron probes. Glass analyses were obtained using a 15 kV acceleration voltage, 10 nA beam current, and a defocused 5–15 μm beam. A correction for sodium loss during analysis was made using the online correction scheme and method of Nielsen and Sigurdsson (1981). Natural mineral standards were used for calibration.

XAS Fe^{3+} maps were collected at beamline 13-IDE (GSECARS) at the Advanced Photon Source at Argonne National Lab. 50×50 pixel grids were set up to cover each glass bead with point analyses, with one spot per location. The beam was focused using mutually-orthogonal Kirkpatrick-Baez mirrors to a 1×1 μm area. Incident beam energy was controlled by a water-cooled (9° C) Si(311) channel-cut monochromator. Incident x-ray energy was calibrated on the first derivative peak of an iron metal foil standard (7110.75 eV, Kraft et al., 1996) and no energy drift was detected throughout the analytical session. XAS data were pre-processed using the ATHENA software package (Ravel and Newville, 2005). Data were normalized to the intensity at 7215 eV.

To choose the channels for the maps, we began with subset of the training set used by Dyar et al. (2016b) to predict Fe^{3+}, which contained ~510 channels and 303 spectra – samples from the original dataset with high alkaline contents were excluded due to their inappropriateness for lunar compositions. In the original paper, it was shown that partial least squares provides better accuracy than Lasso when using the entire spectrum. The statistical basis for comparison is cross-validated root mean square error, in which (in this case) the data set was randomly split into 100 sets, one set was held out while the other 99 were used to build a model, and then the samples in the 100^{th} set were predicted. This is repeated 100 times, and the average error for all iterations is reported as RMSE-CV.

In our limited dataset, RMSE-CV values of ±5.3% Fe^{3+} and an internal prediction error (RMSE) of ±4.4% Fe^{3+} were obtained for a 9-component model. This value is slightly different

than in the original Dyar et al. (2016a) paper due to the change in the number of samples, though it still suggests that highly accurate predictions can be universally made for silicate glasses. But those data were acquired at individual locations, requiring ~9 minutes per spectrum, or ~1.06 seconds/channel. By comparison, a Lasso model built to predict $\%Fe^{3+}$ with those data and α = 0.001 yields RMSE-CV = ±7.73% Fe^{3+} and RMSE = ±5.67% Fe^{3+} (α is the hyperparameter that controls how many non-zero β coefficients will be present).

To create maps, we are willing to sacrifice accuracy in the interest of an ability to create visualizations of the redox distribution. Thus, to reduce the number of channels enough to collect maps in a reasonable amount of time, we retrained the Lasso model on the data explained above and tuned the *t* boundary value to reduce the number of channels needed for a prediction to a small enough value (four channels) to allow rapid data collection for a map. The resultant prediction expression is:

$$\%Fe^{3+} = 242.76 - (8.53 \times I_{7118.2}) - (178.30 \times I_{7123.5}) + (85.43 \times I_{7132.2}) - (138.08 \times I_{7215}) \quad (1)$$

where Fe^{3+} is reported as the percentage of the total Fe. In addition, we collected two other data points at 7111.4 eV and 7113.7 eV to capture information in the pre-edge region for Fe^{2+} and Fe^{3+}, respectively. These regression lines with their associated errors are shown in Figure 1. Use of this multivariate analytical technique makes it possible to "map" Fe^{3+} variations using a dense point array and reduces data collection time for a 50×50 pixel grid from 375 hours to ~4.4 hours.

All multivariate models were trained from the XAS results using the open-source machine learning Python library Scikit-learn (Pedregosa et al., 2011) and the Superman website at http://nemo.cs.umass.edu:54321 (Carey et al., 2017). Methods generally follow those used in Dyar et al. (2012a, 2016a, b) and Lanzirotti et al. (2018).

Maps were built using the GSE Mapviewer software created using the Python-based Larch open-source library toolkit for processing and analyzing X-ray spectroscopic and scattering data from synchrotrons (http://cars.uchicago.edu/xraylarch/). It allows visualization and analysis of micro-x-ray fluorescence maps. For each of the 32 glass beads analyzed, maps were created using two different metrics: 1) the Lasso expression given above and 2) the ratio of the peak intensity at 7111.4 eV to that at 7113.7 eV.

RESULTS

Thirty-two glass beads from three different Apollo sites were mapped for this study. These included orange, green, and yellow glasses, as well as both partially crystalline and holohyaline beads (see McCanta et al., 2017 for complete geochemical data). The glass beads exhibited no major element chemical zonation and Fe^{3+} concentrations were not observed to be correlated with any compositional variable studied (i.e., Mg#, TiO_2 content) or with bead diameter. This study focuses on holohyaline beads to exclude any Fe^{3+}/Fe^{2+} fractionation via mineral crystallization.

As our earlier point analysis work suggested (McCanta et al., 2017), a majority of the mapped beads showed no evidence of $Fe^{3+}/\Sigma Fe$ variations within the glass. However, five beads were observed to have measurable differences in $Fe^{3+}/\Sigma Fe$ for both analytical metrics. These included zoning from reduced cores to oxidized rims and oxidized cores to reduced rims (Fig. 2). Glasses with Fe^{3+} zoning showed no concomitant chemical zoning in any other major element such as Mg, total Fe, or Ti and appear uniformly homogeneous (Figs. 2C,F,I).

Several partially crystalline beads from sample 74220 were also mapped (Fig. 3). The lack of Fe^{3+} in the crystallizing phase, olivine, is expected due to crystal chemical controls. The surrounding glass pools appear enriched in Fe^{3+} in comparison to the olivine. Some zoning in

Fe^{3+} is observed within the melt pools with the highest Fe^{3+} concentrations appearing directly in contact with low Fe^{3+} olivine (Fig. 3).

IMPLICATIONS

Geologic: The occurrence of unzoned beads and beads with both oxidized and reduced rims observed in this study can best be explained by considering late-stage magma ascent and eruption conditions. A late-stage oxidation event (Stage 3 in Rutherford et al. (2017)), observed in Ni-rich rims on metal grains in the glass beads, likely results from loss of water from the ascending melt (Rutherford et al, 2017). This produces melt oxidation through the reaction: $4OH = H_2O + H_2 + 1.5O_2$ (Fig. 4). Redox kinetic calculations suggest that oxidation of a melt droplet (diameter = 100 μm) under these conditions takes place in under 1 s (McCanta et al., 2017). Although the unzoned beads have no Fe^{3+} variations, many do contain significant amounts of Fe^{3+} (up to 28% of total Fe) (McCanta et al., 2017) consistent with this oxidation event. Oxidation takes place from the rim inward. Therefore, zoned beads with oxidized rims represent incomplete oxidation prior to the closure temperature, i.e., the glass transition temperature. Zoned beads with reduced rims (Fig. 2) likely represent subsequent reduction either in the lunar vacuum or in the dissipating gas cloud that may have been modestly reducing due to the addition of H^+ from the degassing melt (Fig. 4). This type of H_2 loss due to H_2O dissociation has long been considered the driver of observed oxidation profiles in terrestrial mid-ocean ridge pillow basalts (Christie et al., 1986; Lanzirotti et al., 2018). The increase in Fe^{3+} concentrations observed in MORB pillow basalts via this process (~50%) are similar to those in the lunar glass beads (~47%) with potentially similar pre-eruptive H_2O contents (MORB: 80–950 ppm [e.g., Ito et al., 1983; Hirschmann, 2006]; lunar bead source: 260-1410 ppm [Saal et al., 2008; Hauri et al., 2011]).

The high and variable Fe^{3+} concentrations observed in glass pools in partially crystalline beads (Fig. 3) is likely controlled by olivine crystal chemistry. As Fe^{2+} is preferentially incorporated into the olivine structure (e.g., Canil et al., 1994), Fe^{3+} accumulates in the surrounding melt. Simple fractional crystallization models indicate that crystallization of 30-40% olivine from a melt containing 1% Fe^{3+} initially can raise the Fe^{3+} concentration of the remaining melt by up to 30%. The isolation of the glass pools from each other contributes to the wide range in Fe^{3+} concentrations measured in a single glass bead.

Previous work on lunar glass bead redox was limited to point analyses (McCanta et al., 2017). Although the point analyses were able to identify Fe^{3+} variations within the glass beads, the spatial distribution of these variations remained unknown. The ability to observe the distribution of Fe^{3+} throughout the entire glass bead opens new avenues of study into how far redox reaction fronts have processed (Fig. 2) and how crystallization affects melt composition in the near field (Fig. 3).

Mapping of Fe^{3+} variations in situ: The larger implications of this study relate to the redox mapping presented. This study represents the first time that Fe^{3+} variations have been mapped *in situ* in polished glass samples. This is a huge step forward as it allows for spatial variations in redox gradients in melts to be observed and new geochemical questions to be studied.

This technique is not without complexities. For example, results are dependent on how the data are normalized. This is particularly true for Fe, where concentrations are high so that detector saturation and self-absorption can lead to normalization differences that lead to spurious results. For this reason, the mapping technique can presently be considered at most a qualitative

tool to look for redox gradients; quantitative Fe^{3+} abundances can best be obtained through using more than a few channels in each spectrum.

The multivariate techniques used in this study allow for Fe^{3+} mapping in silicate glasses because there is already an existing XAS glass calibration covering these compositions (Dyar et al., 2016a). XAS analyses of glasses are simpler than those of minerals due to their lack of crystalline structure-driven orientation effects (Dyar et al., 2016b), but we are working to develop calibrations for common liquidus phases in geologic systems. Calibrations of the type required for this type of multivariate analysis currently exist for both garnet (Dyar et al., 2012a) and amphibole (Dyar et al., 2016b) and are in progress for pyroxene (McCanta et al., 2018). With these datasets, mapping of Fe^{3+} variations at the microscale in common mineral phases is now feasible, and accurate in situ measurements of crystal glass partitioning of Fe^{3+} are soon to be feasible. This will allow for development of a better understanding of element fractionation, crystal site occupancy, and oxidation/reduction variations during common geologic processes.

ACKNOWLEDGMENTS

This research was supported by NASA grant NNX16AR18G to M.C.M., NSF grants EAR-1219761 to M.D.D. and -1219850 to M.C.M., and RIS^{4}E, SEEED, and VORTICES nodes of NASA SSERVI. The authors wish to thank Dr. J. Boesenberg and Mr. A. Patchen for their assistance with electron microprobe analyses. The authors also wish to thank the NASA Curation and Analysis Planning Team for Extraterrestrial Materials (CAPTEM) and M. Rutherford for access to the lunar glass beads used in this study.

REFERENCES CITED

Barnes, J.J., Tartèse, R., Anand, M., McCubbin, F.M., Franchi, I.A., Starkey, N.A., and Russell, S.S. (2014) The origin of water in the primitive Moon as revealed by the lunar highlands samples. Earth and Planetary Science Letters, 390, 244-252.

Breitenfeld, L.B., Dyar, M.D., Carey, CJ, Tague, T.J. Jr., and Wang, P. (2018) Predicting olivine composition using Raman spectroscopy through band shift and multivariate analysis. American Mineralogist, in press.

Canil, D., O'Neill, H.St.C., Pearson, D.G., Rudnick, R.L., McDonough, W.F., and Carswell, D.A. (1994) Ferric iron in peridotites and mantle oxidation states. Earth and Planetary Science Letters, 123, 205-220.

Carey, C., Dyar, M.D., Boucher, T., and Giguere, S. (2017) Web-based software for preprocessing, matching, fitting, prediction, and visualization of spectroscopic data: The data exploration, visualization, and analysis of spectra (DEVAS) website. 48th Lunar and Planetary Science Conference, abstract 1097.

Christie, D.M., Carmichael, I.S.E., and Langmuir, C.H. (1986) Oxidation states of mid-ocean ridge basalt glasses. Earth and Planetary Science Letters, 79, 397-411.

Cottrell, E., Kelley, K.A., Lanzirotti, A., and Fisher, R.A. (2009) High-precision determination of iron oxidation state in silicate glasses using XANES. Chemical Geology, 268, 167-179.

Cuikerman, M. and Uhlmann, D.R. (1974) Effects of iron oxidation state on viscosity, lunar composition 15555. Journal of Geophysical Research, 797, 1594-1598.

Dyar, M.D. and Birnie III, D.P. (1984) Quench media effects on iron partitioning and ordering in a lunar glass. Journal of Non-Crystalline Solids, 67, 397-412.

Dyar, M.D., Breves, E.A., Emerson, E., Bell, S.M., Nelms, M., Ozanne, M.V., Peel, S.E., Carmosino, M.L., Tucker, J.M., Gunter, M.E., Delaney, J.S., Lanzirotti, A., and Woodland, A.B. (2012a) Accurate determination of ferric iron in garnets in bulk Mössbauer spectroscopy and synchrotron micro-XANES. American Mineralogist, 97, 1726-1740.

Dyar, M.D., Breves, E.A., Gunter, M.E., Lanzirotti, A., Tucker, J.M., Carey, CJ, Peel, S.E., Brown, E.B., Oberti, R., Lerotic, M., and Delaney, J.S. (2016b) Synchrotron micro-XAS analysis of Fe^{3+} in amphiboles. American Mineralogist 101, 1171-1189.

Dyar, M.D., Carmosino, M.L., Breves, E.A., Ozanne, M.V., Clegg, S.M., and Wiens, R.C. (2012b) Comparison of partial least squares and lasso regression techniques as applied to laser-induced breakdown spectroscopy of geological samples. Spectrochimica Acta Part B, 70, 51-67.

Dyar, M.D., McCanta, M.C., Breves, E.A., Carey, C.J., and Lanzirotti, A. (2016a) Accurate predictions of iron redox state in silicate glasses: A multivariate approach using X-ray absorption spectroscopy. American Mineralogist, 101, 744-748.

Etschmann, Barbara E., Erica Donner, Joël Brugger, Daryl L. Howard, Martin D. de Jonge, David Paterson, Ravi Naidu, Kirk G. Scheckel, Chris G. Ryan, and Enzo Lombi (2014) Speciation mapping of environmental samples using XANES imaging. Environmental Chemistry 11, 341-350.

Filzmoser, P., Gschwandtner, M., and Todorov, V. (2012) Review of sparse methods in regression and classification with application to chemometrics. Journal of Chemometrics, 26, 42-51.

Füri, E., Deloule, E., Gurenko, A., and Marty, B. (2014) New evidence for chondritic lunar water from combined D/H and noble gas analyses of single Apollo 17 volcanic glasses. Icarus, 229, 109-120.

Hafner, S.S., Virgo, D., and Warburton, D. (1971) Oxidation state of iron in plagioclase from lunar basalts. Earth and Planetary Science Letters, 12, 159-166.

Hastie, T., Tibshirani, R., and Friedman, J., 2009. The Elements of Statistical Learning, 2nd Ed. Springer Science, New York, 745 pp.

Hauri, E.H., Saal, A.E., Rutherford, M.C., and Van Orman, J.A. (2015) Water in the Moon's interior: Truth and consequences. Earth and Planetary Science Letters, 409, 252-264.

Hauri, E.H., Weinreich, T., Saal, A.E., Rutherford, M.C., and Van Orman, J.A. (2011) High pre-eruptive water contents preserved in lunar melt inclusions. Science, 333, 213-215.

Hirschmann, M.M. (2006) Water, melting and the deep Earth H_2O cycle. Annual Review of Earth and Planetary Sciences, 34, 629-653.

Huffman, G.P., Schwerer, F.C., Fisher, R.M., and Nagata, T. (1974) Iron distributions and metallic-ferrous ratios for Apollo lunar samples: Mossbauer and magnetic analyses. Proceedings of the 5^{th} lunar conference, 3, 2779-2794.

Hui, H., Peslier, A.H., Zhang, Y., and Neal, C.R. (2013) Water in lunar anorthosites and evidence for a wet early Moon. Nature Geoscience, 6, 177-180.

Ito, E., Harris, D.M., and Anderson, A.T. (1983) Alteration of oceanic crust and geologic cycling of chlorine and water. Geochimica et Cosmochimica Acta, 47, 1613-1624.

Kraft, S., Stumpel, J., Becker, P., and Kuetgens, U. (1996) High resolution x-ray absorption spectroscopy with absolute energy: Calibration for the determination of absorption edge energies. Review of Scientific Instruments, 67, 681-687.

Lanzirotti, A., Dyar, M.D., Sutton, S., Newville, M., Head, E., Carey, C.J., McCanta, M.C., Lee, L., King, P.L., and Jones, J. (2018) Accurate predictions of microscale oxygen barometry in basaltic glasses using V K-edge X-ray absorption spectroscopy: A multivariate approach. American Mineralogist, 103, 1282-1297.

Mayhew, L.E., Webb, S.M. and Templeton, A.S. (2011) Microscale imaging and identification of Fe speciation and distribution during fluid–mineral reactions under highly reducing conditions. Environmental Science and Technology, 45, 4468-4474.

McCanta, M.C., Dyar, M.D., Rutherford, M.J., Lanzirotti, A., Sutton, S.R., and Thomson, B.J. (2017) *In situ* measurement of ferric iron in lunar glass beads using Fe-XAS. Icarus, 285, 95-102.

McCanta, M.C., Dyar, M.D., Steven, C., Gunter, M., and Lanzirotti, A. (2018) *In situ* measurements of Fe^{3+} in pyroxene using x-ray absorption spectroscopy: Using an oriented crystal calibration to refine geothermobarometric calculations. Proceedings of the 49th Lunar and Planetary Science conference, 1074 (abs).

McCubbin, F.M., Steele, A., Hauri, E.H., Nekvasil, H., Yamashita, S., and Hemley, R.J. (2010) Nominally hydrous magmatism on the Moon. Proceedings of the National Academy of Science USA, 107, 11223-11228.

Muñoz, M., De Andrade, V., Vidal, O., Lewin, E., Pascarelli, S., and Susini, J. (2006) Redox and speciation micromapping using dispersive X-ray absorption spectroscopy: Application to iron in chlorite mineral of a metamorphic rock thin section. Geochemistry, Geophysics, Geosystems, 7, doi:10.1029/2006GC001381.

Niebuhr, H.H., Zeira, S., and Hafner, S.S. (1973) Ferric iron in plagioclase crystals from anorthosite 15415. Proceedings of the Lunar Science Conference, 4, 971-982.

Nielsen, C.H. and Sigurdsson, H. (1981) Quantitative methods of electron microprobe analysis of sodium in natural and synthetic glasses. American Mineralogist, 66, 547-552 .

Pedregosa, F., Varoquaux, G., Gramfort, A., Michel, V., Thirion, B., Grisel, O., Blondel, M., Prettenhofer, P., Weiss, R., Dubourg, V., Vanderplas, J., Passos, A., Cournapeau, D., Brucher, M., Perrot, M., and Duchesnay, E. (2011) Scikit-learn: Machine learning in Python. Journal of Machine Learning Research, 2825-2830.

Ravel, B. and Newville, M. (2005) ATHENA, ARTEMIS, HEPHAESTUS: data analysis for x-ray absorption spectroscopy using IFEFFIT. Journal of Synchrotron Radiation, 12, 537-541.

Rutherford, M.J., Head, J.W., Saal, A.E., Hauri, E., and Wilson, L. (2017) Model for the origin, ascent, and eruption of lunar picritic magmas. American Mineralogist, 102, 2045-2053.

Saal, A.E., Hauri, E.H., Lo Cascio, M., Van Orman, J.A., Rutherford, M.J., and Cooper, R.F. (2008) Volatile content of lunar volcanic glasses and the presence of water in the Moon's interior. Nature, 454, 192-195.

Sato, M. (1976) Oxygen fugacity and other thermochemical parameters of Apollo 17 high-Ti basalts and their implications on the reduction mechanism. Proceedings of the Lunar Science Conference VII, 1323-1344.

Schürmann, K. and Hafner, S.S. (1972) On the amount of ferric iron in plagioclases from lunar igneous rocks. Proceedings of the Lunar Science Conference, 3, 615-621.

Tibshirani, R. (1996) Regression shrinkage and selection via the Lasso. Journal of the Royal Statistical Society, Series B, 58, 267-288.

Virgo, D. and Mysen, B.O. (1985) The structural state of iron in oxidized vs. reduced glasses at 1 atm: A ^{57}Fe Mössbauer study. Physics and Chemistry of Minerals, 12, 65-76.

Wilke, M., Farges, F., Petit, P-E., Brown, G.E. Jr., and Martin, F. (2001) Oxidation state and coordination of Fe in minerals: An Fe K-XANES spectroscopic study. American Mineralogist, 86, 714-730.

This is a preprint, the final version is subject to change, of the American Mineralogist (MSA)
Cite as Authors (Year) Title. American Mineralogist, in press.
DOI: https://doi.org/10.2138/am-2019-6863

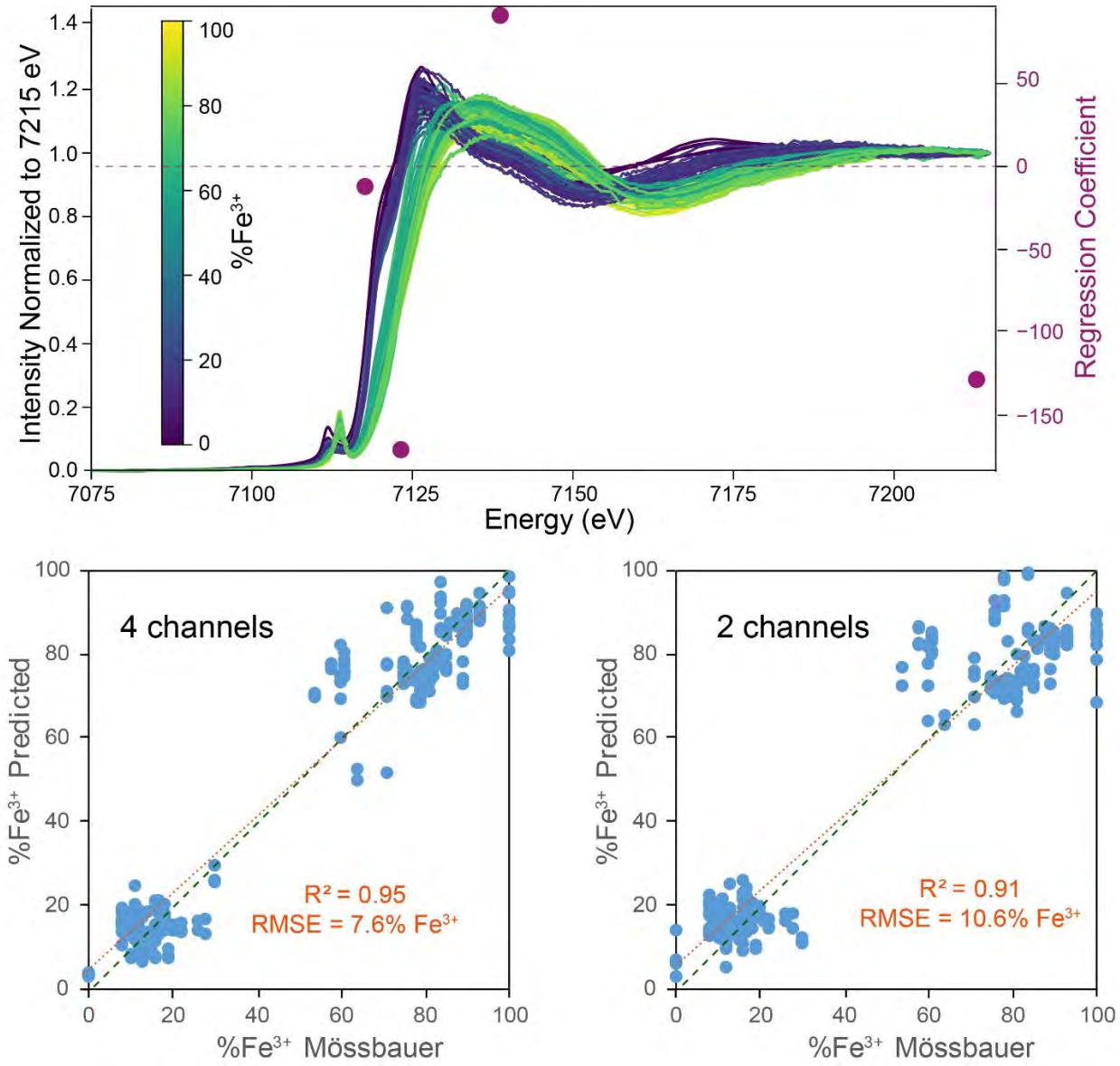

Figure 1. (top) Spectra of 303 silicate glasses color-coded by %Fe^{3+} content as determined by Mössbauer spectroscopy, with locations and magnitudes of regression coefficients indicated in magenta. (bottom) Comparison of predicted vs. Mössbauer %Fe^{3+} content for four-channel (left) and two-channel (right) models. The 1:1 line is shown with dashes and the regression fit line is dotted. RMSE-CV values (which are the magnitude of the *y* axis error bars), while not quite as small as those for the entire spectrum, still show useful values for mapping. Mössbauer error bars are ±1-3%Fe^{3+}.

This is a preprint, the final version is subject to change, of the American Mineralogist (MSA)
Cite as Authors (Year) Title. American Mineralogist, in press.
DOI: https://doi.org/10.2138/am-2019-6863

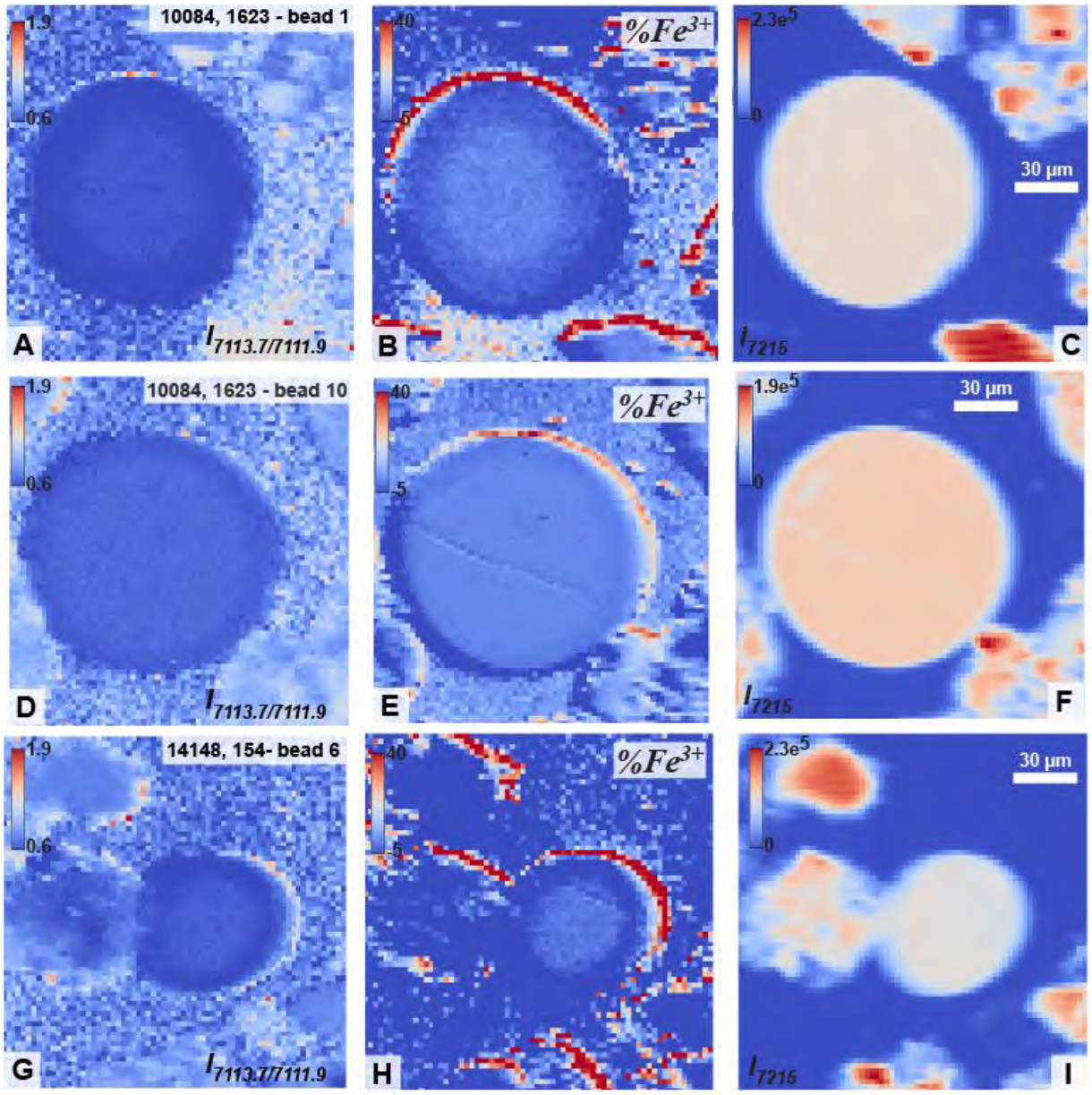

Figure 2. Maps of $Fe^{3+}/\Sigma Fe$ content in holohyaline lunar glass beads from Apollo samples 10084 and 14148. (A-C) 10084,1623 bead 1. (D-F) 10084,1623 bead 10. (G-I) 14148,154 bead 6). Left column: Plotted intensities of the pre-edge peaks, 7113.7/7111.9 eV, with scale bar indicating values of measured ratio. Middle column: Calculated % Fe^{3+} using equation 1 and a scale bar with the values from -5 to +40 % Fe^{3+}. Right column: Measured intensity at 7215, roughly representative of the total Fe content. content.

This is a preprint, the final version is subject to change, of the American Mineralogist (MSA)
Cite as Authors (Year) Title. American Mineralogist, in press.
DOI: https://doi.org/10.2138/am-2019-6863

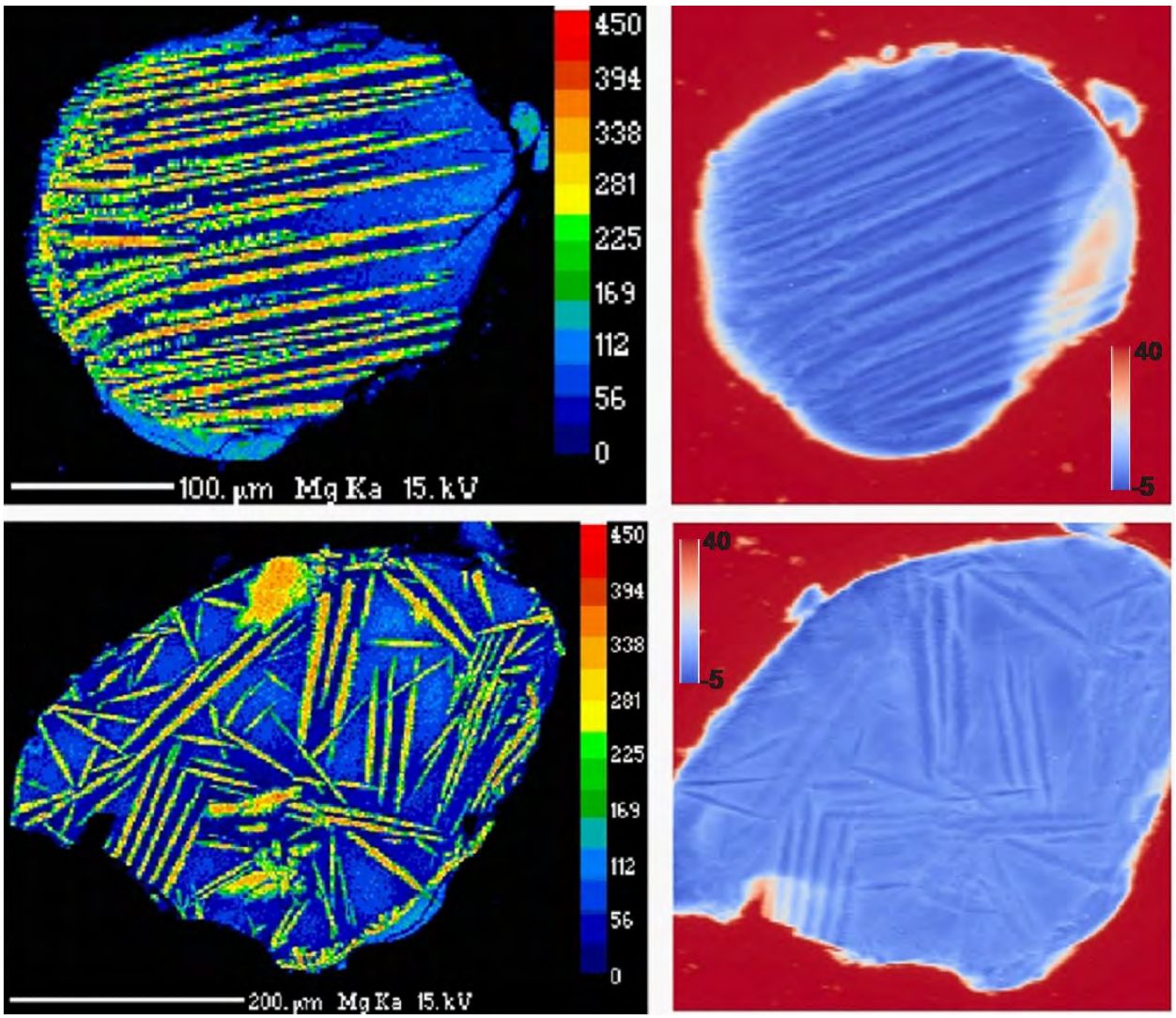

Figure 3. Comparison of maps of electron microprobe Kα Mg content (left) with those of iron redox state (right) in crystalline lunar glass beads from 74220. % Fe^{3+} is calculated using equation 1; scale bar with the values from -5 to +40 % $Fe^{3+}/\Sigma Fe$ is shown. The high Mg minerals crystallizing in these beads are olivine, which incorporates only Fe^{2+}. In the XAS maps, olivine is clearly visible as the darker blue material with little/no Fe^{3+}, while the surrounding melt contains more Fe^{3+}.

This is a preprint, the final version is subject to change, of the American Mineralogist (MSA)
Cite as Authors (Year) Title. American Mineralogist, in press.
DOI: https://doi.org/10.2138/am-2019-6863

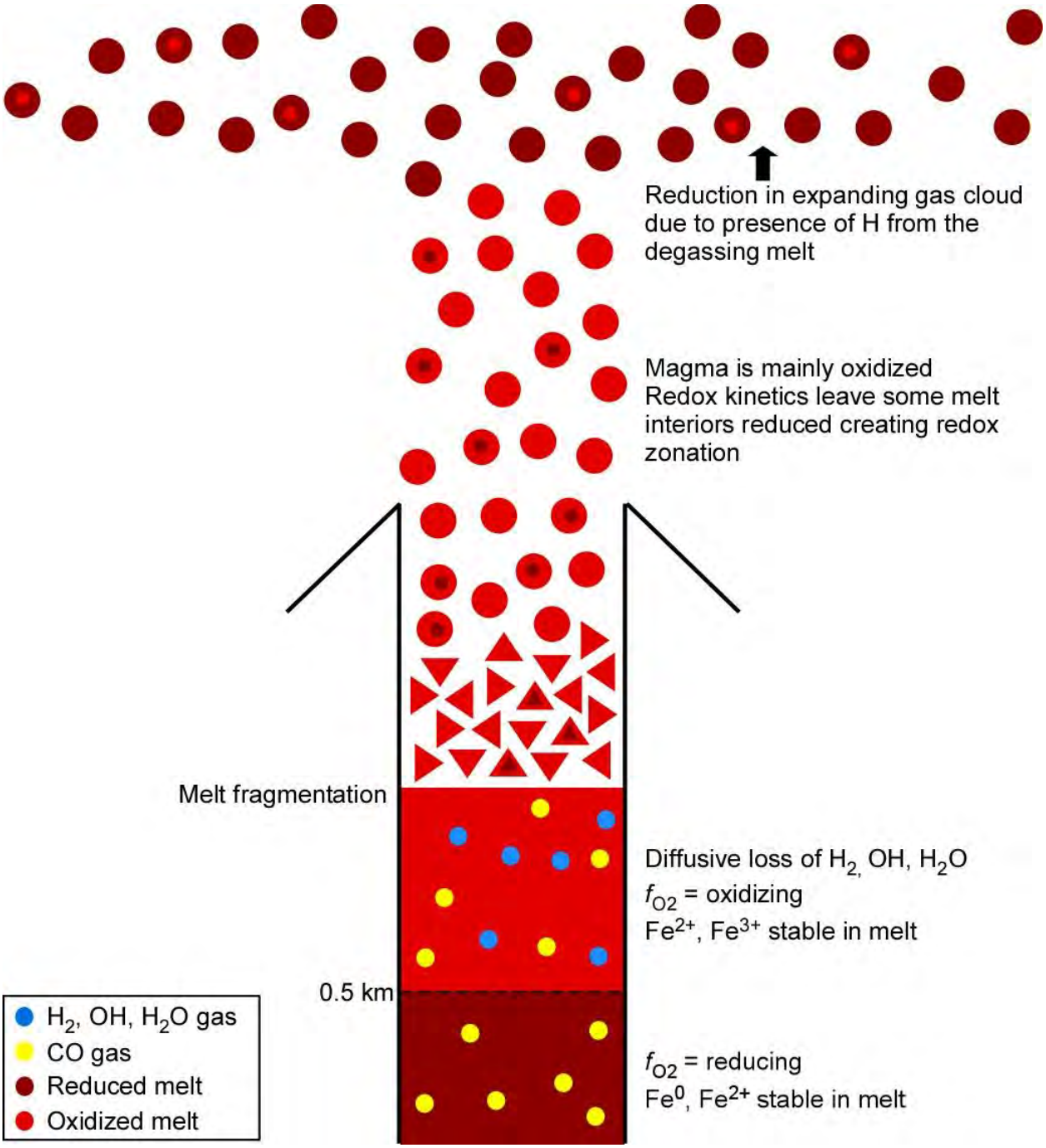

Figure 4. Cartoon of the oxidation/reduction environments in the melt column during ascent and eruption.